Global effects on neoclassical transport in the pedestal with impurities

I. Pusztai,[1, a)] S. Buller,[1] and M. Landreman[2]
[1)] *Department of Physics, Chalmers University of Technology, SE-41296 Göteborg, Sweden*
[2)] *Institute for Research in Electronics and Applied Physics, University of Maryland, College Park, MD 20742, USA.*

(Dated: 1 July 2016)

We present a numerical study of collisional transport in a tokamak pedestal in the presence of non-trace impurities, using the radially global δf neoclassical solver PERFECT [M. Landreman et al. 2014 *Plasma Phys. Control. Fusion* **56** 045005]. It is known that in a tokamak core with non-trace impurities present the radial impurity flux opposes the bulk ion flux to provide an ambipolar particle transport, with the electron transport being negligibly small. However, in a sharp density pedestal with sub-sonic ion flows the electron transport can be comparable to the ion and impurity flows. Furthermore, the neoclassical particle transport is not intrinsically ambipolar, and the non-ambipolarity of the fluxes extends outside the pedestal region by the radial coupling of the perturbations. The neoclassical momentum transport, which is finite in the presence of ion orbit-width scale profile variations, is significantly enhanced when impurities are present in non-trace quantities, even if the total parallel mass flow is dominated by the bulk ions.

PACS numbers:
Keywords:

arXiv:1603.00688v3 [physics.plasm-ph] 30 Jun 2016

I. INTRODUCTION

The global confinement in tokamaks is strongly correlated with the performance indicators of the edge transport barrier[1,2]. Accordingly, having a good pedestal performance in a fusion reactor is considered to be crucial. In the pedestal, turbulent transport is dramatically reduced by decorrelation of turbulence by strong sheared flows[3,4], thus the relative role of the (otherwise negligible) collisional transport becomes more important.

Fusion reactors will need to operate with carbon-free and low-erosion plasma facing components to achieve reasonable lifetimes and for nuclear safety. To gain more operational experience in the proposed metallic wall devices, originally carbon walled tokamak experiments, such as JET and ASDEX have transitioned to operation with "ITER-like walls" (with Be and W components) in recent years. With this transition a global confinement degradation has been observed[5,6], especially on JET. This is a serious concern, since the data on which experimental scaling relations (and projections for ITER) are based have been mostly collected on carbon wall experiments. This degradation is found to be primarily caused by reduced pedestal performance[5,6]. Impurity injection appears to have a beneficial effect in certain cases[7]. Over and above the general importance of collisional impurity transport, these observations motivate consideration of the effects of non-trace impurities in the pedestal.

Modeling of neoclassical transport in the pedestal is difficult, since the very sharp profile variations make gradient scale lengths comparable to the radial extent of the ion drift orbits[8], which renders the usual radially local modeling inadequate for the problem. It has been demonstrated analytically that finite orbit width effects can significantly modify neoclassical transport phenomena[9–14], producing modified ion heat transport, flows, bootstrap current, and even zonal flow response. These studies are limited to large aspect-ratio, circular cross-section plasmas and describe profile variations mostly through local plasma parameters, and point at the importance of a short scale global variation of flows[14]. In this paper we go beyond the large aspect-ratio limit, and present a radially global numerical study of neoclassical transport in the presence of non-trace impurities.

There are different possible modeling options of various sophistication and difficulty. The simplest option is the computationally cheap and usually adopted *local* δf formalism, which assumes small orbit width compared to profile length scales and neglects the radial coupling of the perturbations. On the other end, the *global full-f* approach includes both neoclassical and turbulent transport (these transport channels cannot be completely decoupled in a pedestal, in contrast to the local limit) and allows for strong deviations from local thermodynamic equilibrium. This approach requires nonlinear collision operators to fully live up to its promises[15], and is currently numerically too expensive to be used for exploratory studies[16,17]. In this work, we use the *global* δf formalism[18]. This is a specific generalization of the local δf formalism which includes global effects, while still allowing the distribution function to be linearized around an appropriately chosen lowest order Maxwellian. This linearization, which assumes sub-sonic parallel flows, imposes limitations on the profiles that can be considered. Accordingly, we restrict ourselves to using suitable model profiles, but with experimentally identifiable features.

In core plasmas the neoclassical perturbations of the ion distribution are only weakly affected by the electrons.

[a)] Electronic mail: pusztai@chalmers.se

We find that neoclassical particle transport in a pedestal with subsonic ion flows can be very different from that in the plasma core (Fig. 2a-c): The electron particle flux can be comparable to the ion particle flux even in the presence of non-trace impurities, and the collisional particle transport is not ambipolar in general. Consequently, it can happen that ions and impurities are transported in the same direction. In the presence of sharp profile variations the neoclassical momentum transport is nonzero, and we observe that its magnitude is notably affected by non-trace impurities (Fig. 8a).

The remainder of this paper is organized as follows. In Sec. II, we describe the global δf method implemented in PERFECT, and how this affects our choice of model profiles. In Sec. III we first present the neoclassical fluxes, flows and poloidal density variations for our baseline case, and then compare the results between plasmas with trace and non-trace impurity content. Finally, in Sec. IV we discuss our results and conclude.

II. METHODS

In a tokamak core the plasma parameter profiles often exhibit sufficiently slow radial variations that the departure of the distribution function from a Maxwellian remains small, and the collisional dynamics can be described in terms of local plasma parameters. In this situation neoclassical transport can be calculated using the local δf formalism that yields a linear system for the perturbed distribution. If the driving radial gradients are strong enough to generate substantial parallel particle flows, and poloidal variation in plasma parameters, the problem becomes nonlinear[19]. Furthermore, if all plasma parameters are allowed to vary over a radial width of a typical ion orbit, the transport becomes radially non-local. To study such general situations a global full-f simulation code with a nonlinear collision operator would be necessary. While a limited number of such simulation codes exist[16,20,21], their computational expense make them unfit for our exploratory purposes. To keep the problem tractable, we will only consider situations when the distribution functions are not far from Maxwell-Boltzmann distributions, but finite orbit width effects are still important. For this purpose, we use the radially global, δf, Eulerian neoclassical solver PERFECT.

The fact that the distribution functions must be close to Maxwellians puts constraints on the profiles, as will be discussed in the following section. These constraints might not typically be satisfied in an experiment. Therefore, we do not attempt to base our exploratory modeling on specific experimental profiles, instead we use model profiles chosen specifically to satisfy the assumptions in PERFECT, while they are supposed to be representative of experimental profiles in some respects. The specific profiles we use are presented in Appendix A. To explain the origin of the constraints, the next section contains a brief summary of the equations solved in PERFECT (for a more detailed description of the code, we refer the reader to 18).

In addition to the constraints outlined below, PERFECT does not capture the geometry of an X-point or the open field line region. Orbit losses[22] and an influx of neutral atoms[23] are expected to become important very close to the separatrix. For this reason we expect that our results are representative only of the inner part of the pedestal.

A. The global δf problem solved by PERFECT

PERFECT solves for the non-adiabatic perturbed distribution function

$$g_a = f_a - f_{Ma} + \frac{e_a \Phi_1}{T_a} f_{Ma}, \tag{1}$$

where f_a is the distribution function, e_a is the charge, and T_a is the temperature of species a, $\Phi_1 = \Phi - \Phi_0$ is the perturbed potential, with the unperturbed electrostatic potential Φ_0 taken to be a flux function, $\Phi_0 = \langle \Phi \rangle$. The flux surface average is defined as $\langle X \rangle = \int_0^{2\pi} X d\theta (\boldsymbol{B} \cdot \nabla\theta)^{-1} / \int_0^{2\pi} d\theta (\boldsymbol{B} \cdot \nabla\theta)^{-1}$, where θ is a 2π-periodic angle-like poloidal coordinate and $\boldsymbol{B}$ is the magnetic field. The perturbation g_a is required to be small compared to the lowest order distribution function, which is a Maxwell-Boltzmann distribution

$$f_{Ma}(\psi, W_{a0}) = \eta_a(\psi) \left(\frac{m_a}{2\pi T_a(\psi)} \right)^{3/2} e^{-\frac{m_a W_{a0}}{T_a(\psi)}}, \tag{2}$$

where the radial coordinate ψ is $1/(2\pi)$ times the poloidal magnetic flux, m_a is the mass, $m_a W_{a0} = m_a v^2/2 + e_a \Phi_0$ is the total unperturbed energy, and $\eta_a = n_a(\psi) e^{e_a \Phi_0(\psi)/T_a(\psi)}$ is the pseudo-density, with the density n_a. The linearized equation that PERFECT solves is

$$\begin{aligned} \left(v_\parallel \boldsymbol{b} + \boldsymbol{v}_{da0}\right) \cdot (\nabla g_a) - C_{la}(g_a) - S_a \\ = -\boldsymbol{v}_{ma} \cdot \nabla\psi \left(\frac{\partial f_{Ma}}{\partial \psi} \right), \end{aligned} \tag{3}$$

[18]

where $\boldsymbol{b} = \boldsymbol{B}/|\boldsymbol{B}|$, $v_\parallel = \boldsymbol{v} \cdot \boldsymbol{b}$ with the velocity $\boldsymbol{v}$, the lowest order drift velocity $\boldsymbol{v}_{da0}$ contains the lowest order $E \times B$ drift and magnetic drifts $\boldsymbol{v}_{ma}$, C_{la} is the linearized Fokker-Planck operator, and S_a is a source term, which will be explained shortly. The partial derivatives are taken at fixed magnetic moment $\mu_a = m_a v^2/(2B)$ and unperturbed total energy W_{a0}.

Note that boundary conditions in ψ are needed to fully specify g_a by (3), in contrast to the local equation. Since the local theory should apply sufficiently far from the pedestal, the result of local simulations – in which the $\boldsymbol{v}_{da0} \cdot (\nabla g_a)_{\mu, W_{a0}}$ term is dropped from (3) – are imposed as boundary conditions where particles enter the domain[18].

As inputs, PERFECT requires zeroth order (flux function) densities n_a, temperature T_a and potential Φ_0. Given these equilibrium profiles, g_a is calculated from (3), and appropriate velocity moments of g_a provide the neoclassical flows and fluxes. The fluxes will in general not be divergence free and thus incompatible with the time-independent equilibrium profiles. It may seem instructive to restore the time derivative in (3), and solve a time-dependent problem, in a hope to reach a steady state equilibrium. However, only exceptional profiles would lead to a steady state solution. More generally, particles and energy would accumulate in (or leave) the simulation domain until the δf approach breaks down. Instead, the approach adopted is to add spatially varying sources S_a so that the zeroth-order profiles become consistent; these sources are solved for in the code alongside g_a. These sources can be thought of as representing the effects of non-neoclassical transport needed to make the profiles consistent, and should also be present in a real pedestal.

To guarantee that $g_a \ll f_a$, the driving gradients in the right-hand side of (3) should remain small. From

$$\left.\frac{\partial f_{Ma}}{\partial \psi}\right|_{W_{a0}} = \left[\frac{\eta_a'}{\eta_a} + \left(\frac{m_a W_{a0}}{T_a} - \frac{3}{2}\right)\frac{T_a'}{T_a}\right] f_{Ma}, \qquad (4)$$

where prime denotes the ψ-derivative, we see that the η and temperature gradients set the size of g_a, and thus drive the deviations from a Maxwellian. Hence the density and the electrostatic potential may have sharp gradients as long as they produce a slowly varying η. To quantify what we mean by a sharp gradient, we may balance the $v_\parallel \boldsymbol{b}\cdot\nabla g_a$ and $\boldsymbol{v}_{ma}\cdot\nabla\psi\partial_\psi f_{Ma}$ terms in (3) to find that

$$\rho_{pa}|\nabla\psi|(\log X)' \ll 1 \qquad (5)$$

should be satisfied by T_a and η_a; that is, these quantities should have a small relative change as experienced by a particle during its radial drift excursion. Here $\rho_{pa} = v_a m_a/(e_a B_p)$ is the poloidal Larmor radius of the species, with the thermal speed $v_a = \sqrt{2T_a/m_a}$, and the poloidal magnetic field $B_p = \boldsymbol{B}\cdot\nabla\theta/|\nabla\theta|$.

B. Model profiles and magnetic geometry

Although we would like to use pedestal profiles which are representative of experiments in some aspects, we require (5) to be satisfied in the simulations for all species ($a = \{e, i, z\}$ for electrons, ions and impurities, respectively). We consider pedestals where n_a and T_e are allowed to vary on the ρ_{pi} scale, while the T and η gradients of the bulk and impurity ion species are constrained by (5).

As a starting point we considered profiles from typical JET discharges (Figure 16 of 24), and modified them as necessary to satisfy our orderings, and to reduce the need for heat sources in the simulation domain. The specific choices made in constructing the model profiles

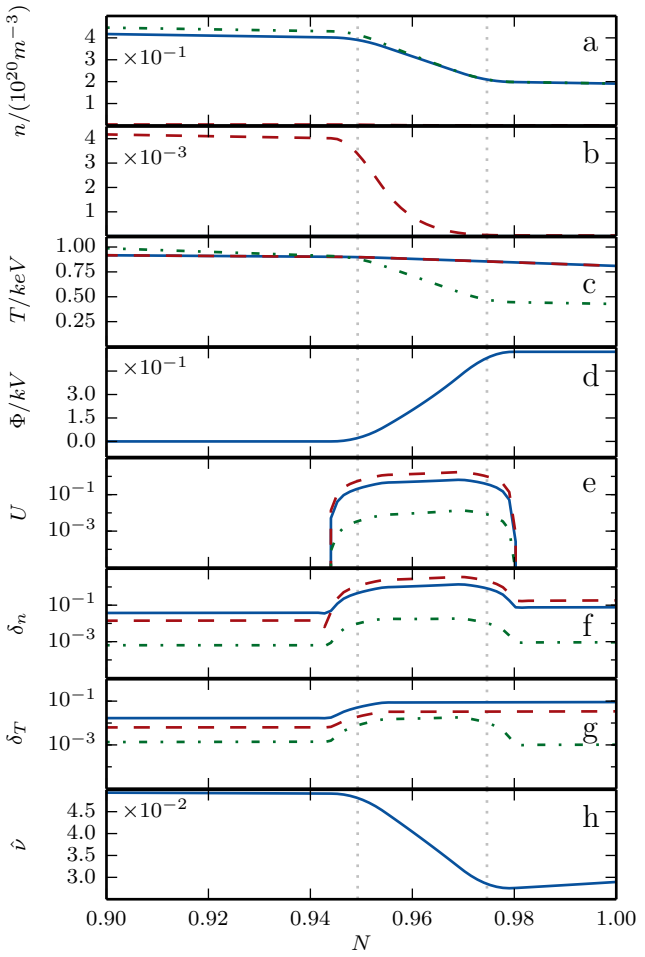

FIG. 1: Ion (solid curve), impurity (dashed) and electron (dash-dotted) input profiles (a-d) and derived quantities (e-h) for the baseline simulation.

are discussed in Appendix A. The resulting input profiles for our baseline case as functions of the normalized poloidal flux ψ_N are shown in Fig. 1a-d. Here, we introduced $\psi_N = \psi/\psi_{\mathrm{LCFS}}$, where ψ_{LCFS} is the poloidal flux at the last closed flux surface (LCFS). Note that the density profile of impurities is much steeper than that of the bulk ions to make η_z vary slowly. We consider a deuterium plasma and fully ionized nitrogen impurities ($Z_z = 7$, where $Z_a = e_a/|e_e|$) with a concentration $n_z/n_i = 0.01$ in the core. The radii marking the beginning and the end of the pedestal are indicated by dotted vertical lines in the figures.

In the simulations we use a local Miller model geometry[25] (and neglect the radial variation of B_p and $B_t = \sqrt{|\mathbf{B}|^2 - B_p^2}$ in the domain), with elongation $\kappa = 1.58$, $s_\kappa \equiv (r/\kappa)\mathrm{d}\kappa/\mathrm{d}r = 0.479$, triangularity $\delta = 0.24$, $s_\delta \equiv (r/\sqrt{1-\delta^2})\mathrm{d}\delta/\mathrm{d}r = 0.845$, $\partial R/\partial r = -0.14$, $q = 3.5$, and inverse aspect ratio $\epsilon \equiv r/R = 0.263$, with r and R denoting the minor and major radii, respectively. These parameters were taken from 26.

The numerical resolution and convergence tests are detailed in Appendix B.

C. Units

An input quantity X is supplied to PERFECT in a normalized, dimensionless form $\hat{X} = X/\bar{X}$, with the normalizing, dimensional quantity $\bar{X}$. We choose $\bar{R} = 3.8\,\mathrm{m}$ and $\bar{B} = 2.9\,\mathrm{T}$ to be the major radius and magnetic field at the magnetic axis. Furthermore we choose the following convenient units $\bar{n} = 10^{20}\,\mathrm{m}^{-3}$, $\bar{T} = e\bar{\Phi} = 1\,\mathrm{keV}$, $\bar{m} = m_D$ (deuterium mass), and $\bar{e}$ is the elementary charge. We define the reference speed and collision frequency as $\bar{v} = \sqrt{2\bar{T}/\bar{m}}$ and

$$\bar{\nu} = \frac{\sqrt{2}}{12\pi^{3/2}} \frac{e^4 \bar{n} \ln\Lambda}{\epsilon_0^2 \sqrt{\bar{m}} \bar{T}^{3/2}}, \tag{6}$$

where ϵ_0 denotes the vacuum permittivity and $\ln\Lambda$ is the Coulomb logarithm. The ordinary same-species collision frequency ν_{aa} is defined as (6) but with $\bar{T}$ and $\bar{n}$ replaced by T_a and n_a, from which we may define the collisionality as $\hat{\nu}_{aa} = \nu_{aa} q R/v_a$.

To quantify when the local approximation fails, it is useful to define a few additional quantities: The normalized electric field $U_a = I/(Bv_a)\,\mathrm{d}\Phi_0/\mathrm{d}\psi$ measures how much the $E \times B$ drift competes with parallel streaming in terms of poloidal particle motion. The normalized logarithmic derivative $\delta_X = -Iv_a/(\Omega_a)\,\mathrm{d}(\ln X)/\mathrm{d}\psi$ measures the variation of quantity X along a typical drift orbit, where $\Omega_a = e_a B/m_a$ and $I = RB_t$. Local neoclassical theory is valid only when U, δ_n, δ_η, and δ_T are all much smaller than unity in magnitude. The global δf model also requires that $|\delta_T| \ll 1$ and $|\delta_\eta| \ll 1$, but U and δ_n can be $\mathcal{O}(1)$. These derived quantities together with $\hat{\nu}$ are shown for the baseline profiles in Fig. 1e-h.

III. LOCAL AND GLOBAL SIMULATION RESULTS

To study the differences between local and global neoclassical transport we performed a number of PERFECT simulations with the profiles and magnetic geometry described in Sec. II B. Before presenting the simulation results for our baseline set of profiles, we discuss the output quantities.

We define the following normalized output quantities: sources, $\hat{S}_a = \bar{v}^2 \bar{R} S_a/(\Delta \bar{n} \hat{m}_a^{3/2})$, with $\Delta = \bar{m}\bar{v}/(\bar{e}\bar{B}\bar{R})$; $\hat{V}' = V'\bar{B}/\bar{R}$, with $V' = \oint d\theta/|\boldsymbol{B}\cdot\nabla\theta|$; particle flux, $\hat{\boldsymbol{\Gamma}}_a = \int d^3v g_a \boldsymbol{v}_{ma}/(\bar{n}\bar{v})$; momentum flux (divided by mass), $\hat{\boldsymbol{\Pi}}_a = \int d^3v g_a v_\parallel I \boldsymbol{v}_{ma}/(\bar{n}\bar{v}^2\bar{R}B)$; heat flux, $\hat{\boldsymbol{Q}}_a = \int d^3v g_a m_a v^2 \boldsymbol{v}_{ma}/(2\bar{T}\bar{n}\bar{v})$; conductive heat fluxes, $\hat{\boldsymbol{q}}_a = \hat{\boldsymbol{Q}}_a - (5/2)\hat{T}\hat{\boldsymbol{\Gamma}}_a$; parallel flow velocity, $\hat{V}_{\parallel a} = \int d^3v v_\parallel g_a/(\bar{v}\Delta n_a)$; parallel current, $\hat{J}_\parallel = \sum_a Z_a \hat{n}_a \hat{V}_{\parallel a}$. The neoclassical flow coefficient $k_\parallel$ is defined so that it reduces to the flux function poloidal flow coefficient for a single ion species plasma in the local limit,

$$k_\parallel = \left(\frac{\mathrm{d}T}{\mathrm{d}\psi}\right)^{-1} \frac{\langle B^2\rangle}{B^2} \left(\frac{e_a B}{I} V_{\parallel,a} + \frac{1}{n_a}\frac{\mathrm{d}p_a}{\mathrm{d}\psi} + e_a \frac{\mathrm{d}\Phi}{\mathrm{d}\psi}\right), \tag{7}$$

where $p_a = n_a T_a$ is the pressure. Furthermore, we define the non-adiabatic density perturbation $\tilde{n}_a^{(g)} = \int d^3v g_a$, the total density perturbation $\tilde{n}_a = \int d^3v (f_a - f_{Ma})$, and normalized scalar fluxes

$$\hat{F}_a = \frac{\hat{\psi}_a \hat{V}' \bar{R}}{\Delta^2 \pi} \langle \hat{\boldsymbol{F}}_a \cdot \nabla\psi_N \rangle, \tag{8}$$

with $\hat{F}_a$ ($\hat{\boldsymbol{F}}_a$) representing $\hat{\Gamma}_a$, $\hat{q}_a$ or $\hat{\Pi}_a$ ($\hat{\boldsymbol{\Gamma}}_a$, $\hat{\boldsymbol{q}}_a$ or $\hat{\boldsymbol{\Pi}}_a$, respectively), and $\hat{\psi}_a = \psi_{\mathrm{LCFS}}/(\bar{R}^2\bar{B})$. Note that the flux normalizations are species independent.

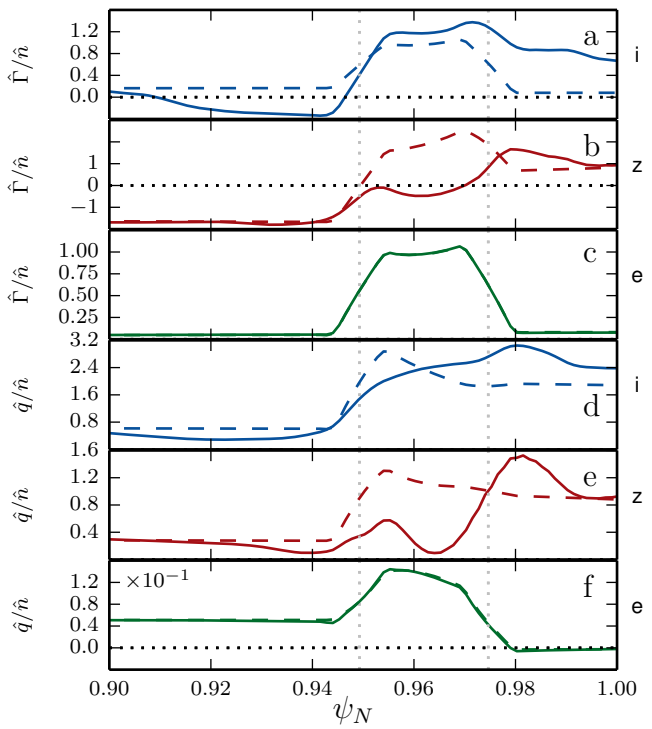

FIG. 2: Particle (a-c) and heat fluxes (d-f) divided by the normalized density, where the different subplots show the fluxes for different species. Solid (dashed) lines represent global (local) simulations. Species is indicated to the right of the panels.

A. Results for the baseline case

The scalar fluxes of (8) divided by $\hat{n}$ are shown in Fig. 2. Throughout Sec. III solid lines represent global simulation results, and dashed lines represent local ones.

When the impurity strength $\alpha = Z_{\mathrm{eff}} - 1$ is order unity – as in our baseline – the magnitude of the particle transport of electrons is typically $\sqrt{m_e/m_i}/\alpha$ smaller than

that of the impurities, where $Z_{\rm eff}$ denotes the effective ion charge. In this case it is common to neglect $\hat{\Gamma}_e$ and calculate the ion particle transport from ambipolarity $\sum_{a\neq e} Z_a \hat{\Gamma}_a = 0$, leading to opposing ion and impurity particle fluxes. The local simulations in the core region obey these expectations. Since $\mathrm{d}T_i/\mathrm{d}\psi$ is small in our baseline, temperature screening does not dominate, thus the local fluxes obey $\hat{\Gamma}_i > 0$ and $\hat{\Gamma}_z < 0$. In the pedestal the parallel ion-electron friction can be sufficiently large to compete with the ion-impurity friction, due to the high electron flow speeds. Therefore $\hat{\Gamma}_e$ cannot be neglected anymore in the ambipolarity condition: the strong outward electron flux means that both $\hat{\Gamma}_z$ and $\hat{\Gamma}_i$ are positive simultaneously. Thus the outward local $\hat{\Gamma}_z$ is not a result of temperature screening.

As expected from the small U_e and δ_{ne} values, seen in Fig. 1e and f, the electron local and global fluxes are practically the same. However, finite orbit width effects strongly affect the ion and impurity dynamics. In the pedestal $\hat{\Gamma}_i$ is increased compared to the local value, which causes $\hat{\Gamma}_z$ to change sign compared to its local value. It is worth noting that the deviation between local and global results is not localized to the pedestal region only. For instance, the global and local $\hat{\Gamma}_i$ deviate well below $\psi_N = 0.94$; the ion particle flux changes sign at $\psi_N = 0.91$ while the local result is positive everywhere. As a comparison we note, that the width of the large gradient region in ψ_N units is approximately 0.026, and the orbit width of a typical trapped ion at thermal speed is 0.016.

The somewhat surprising observation that the finite orbit width effects extend outside the pedestal over several thermal ion orbit widths is worth a moment of thought. Since the existing analytical theories assume $\sqrt{\epsilon} \ll 1$, which partly eliminates the radial coupling, they can only provide a limited guidance as to why this happens. The only radial coupling that cannot be completely eliminated from those theories is that due to the neoclassical parallel flow, $k_\parallel$; indeed it is not a parameter in the theory, but it satisfies a radial differential equation (Eqs. (43) and (64) in Ref. 14). As we will see, in our case the global result for the main ion $k_\parallel$ is very different from the local one, and it takes a rather long distance from the pedestal before it gets close to the local result. Also, in estimating the orbit width above, we considered particles at the thermal speed, while all the quantities of interest are dominated by super-thermal particles with wider orbits. The neoclassical drive and the radial coupling terms both include $\boldsymbol{v}_m \cdot \nabla\psi \propto v^2$, the velocity space integration weight is $\propto v^2$, and the flow, particle flux, and heat flux contain an additional factor of v, v^2, or v^4 respectively.

The global particle fluxes are not ambipolar as seen at $\psi_N = 0.94$, where $\hat{\Gamma}_i$ and $\hat{\Gamma}_z$ are both inward, and $\hat{\Gamma}_e$ is small, very close to its local value. Note that while in a local simulation the radial current and momentum flux should vanish, it does not need to be so in global simulations, as pointed out in 18.

For both ions and impurities we observe that the conductive heat flux can significantly differ from the local value. A reduction compared to the the local value – observed around the pedestal top – may be explained by the shift of the trapped region towards the tail of the distribution at $U \sim 1$. However, we also find regions where the heat fluxes increase from their local values. Just as for the particle fluxes, we see a reduction inside the pedestal top: $\hat{q}_i$ ($\hat{q}_z$) reaches a minimum at $\psi_N \approx 0.92$ ($\psi_N \approx 0.94$).

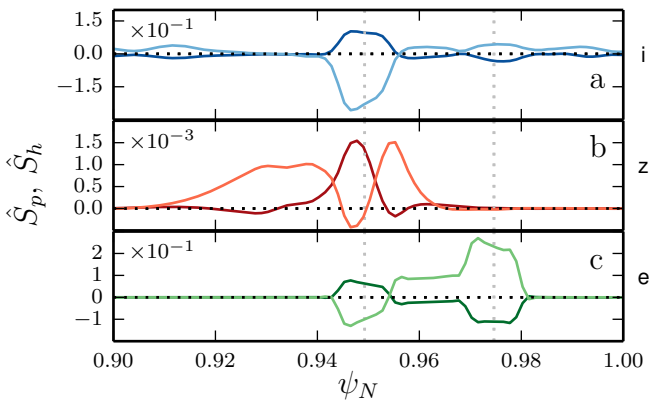

FIG. 3: Particle (dark curves) and heat (light curves) sources for the various species. Species is indicated to the right of the panels.

The corresponding sources are presented in Fig. 3. We use poloidally symmetric sources with speed dependencies $(x_a^2 - \{5,3\}/2)\exp(-x_a^2)$ for particle and heat sources, respectively, where $x_a = v/v_a$. We see that to some degree the main ion particle and heat sources qualitatively mirror each other, and tend towards zero outside the pedestal. We specifically choose T_i to reduce the need for S_{hi}, while S_{pi} also remains small, because $\hat{\Gamma}_i$ tends to be smaller than $\hat{q}_i$. The tremendous drop in $\hat{n}_z$ in the pedestal leads to a sharp peak in S_{pz}, and again we see an opposing trend for S_{hz}, but for impurities the combined sources are positive. The electron sources are localized to the pedestal and comparable in size to those of the main ions.

The neoclassical flow coefficients, $k_\parallel$, are presented in Fig. 4. The local (dashed lines) $k_{\parallel i}$ is positive as expected in the banana regime, and exhibits a slight variation as a response to the radial variation of $\hat{\nu}$. In the local case $k_\parallel$ is a flux function, while globally it varies from the inboard side (darker curves) to the outboard side (lighter curves). These poloidal variations in the flow appear together with poloidal density variations, as will be discussed shortly. It has been shown analytically[10,12,14] that $k_\parallel$ is affected by finite orbit width effects. As seen from the analytical results, where $\boldsymbol{v}_{da0} \cdot \nabla\theta$ is kept but the radial coupling is neglected, $k_\parallel$ is expected to decrease or become more negative in both the banana and plateau regimes[10,12]. However, the global modification to $k_\parallel$ is not a function of local plasma parameters (such as U_a) only, but even in the semi-global treatment of 14 it satisfies a radial

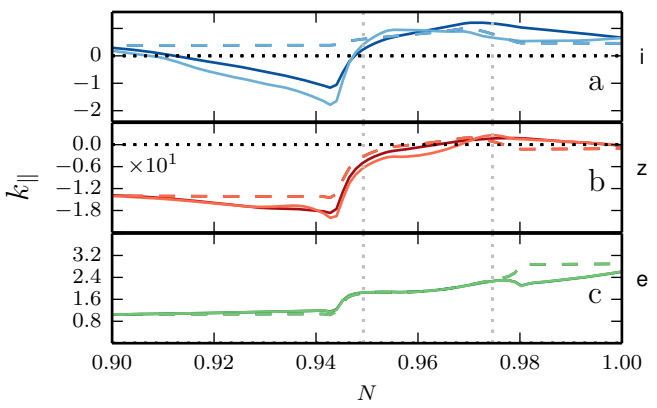

FIG. 4: $k_\parallel$, defined in (7), with darker lines being $k_\parallel$ at the inboard side, $\theta = \pi$, lighter at $\theta = 0$; dashed lines show the results of corresponding local simulations (the outboard and inboard curves overlap). Species is indicated to the right of the panels.

differential equation (i.e. $\partial g/\partial\psi$ cannot be neglected). This is why $k_\parallel$ can differ in sign and magnitude from the local value well outside the pedestal, and can be larger than its local value inside the pedestal. It is interesting to note that there is a difference between global and local $k_\parallel$ even for the electrons, which is due to the collisional coupling to the various ion species.

The density perturbations are shown in Fig. 5. We first consider only the non-adiabatic contribution to the perturbations, $\tilde{n}_a^{(g)}/n_a$, shown in Fig. 5a-f, where the global (local) results are plotted in the a-c (d-f) panels. The local simulations predict purely up-down density asymmetry for all species, which is weaker for bulk ions and electrons than for impurities. The global results show a more complex poloidal density variation for both ions and impurities. For ions we see an in-out asymmetry (i.e. excess density around $\theta = \pi$) at the pedestal top, which transforms into an out-in asymmetry in the pedestal, and reverses again further out (similarly to the single species simulations of 27). For impurities the most important difference compared to the local results is the weak in-out (instead of strong up-down) asymmetry in the pedestal. The electron density perturbation mostly follows its local behavior, exhibiting a large increase in the up-down asymmetry in the pedestal. To understand the total density perturbation $\tilde{n}_a/n_a$ in global simulations we note that the potential perturbation Φ_1 follows mostly the non-adiabatic ion density perturbation. The total electron density perturbation is dominated by the adiabatic response of electrons, thus it is very similar to the ion density perturbation. The impurity density variations show a competition between adiabatic response – especially in the pedestal where it tries to oppose the ion density perturbation – and non-adiabatic response. The relative impurity density variation stays below 10% everywhere, showing that the assumption of the density being nearly a flux function is not violated. However, for

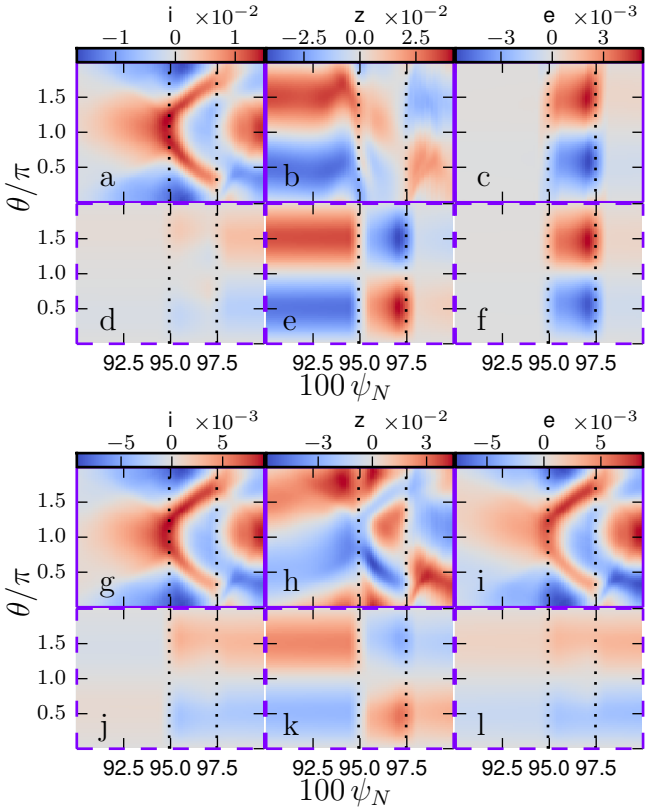

FIG. 5: The non-adiabatic contribution to the density perturbation (a-f), and the total density perturbation (g-l). Dashed frame (d-f and j-l) indicates local results. Species is indicated above the panels.

sufficiently high Z_z, nonlinearity from poloidal asymmetries can arise[19,28,29].

Finally, we consider the parallel flows and the bootstrap current for our baseline case; these are plotted in Fig. 6. For the bulk and impurity ions the flows remain small inside the pedestal, as their profiles were chosen specifically so that their diamagnetic and $E \times B$ flows mostly cancel. For these the relative deviation between the local and global results is significant, the global results being larger in magnitude from the middle of the pedestal inward. This is partly due to the reduction in $k_\parallel$ compared to the local value observed in Fig. 4. The parallel flow of electrons reaches a much higher magnitude inside the pedestal then that of the ions, where the strong $E \times B$ and diamagnetic rotation contribute with the same sign for this species. The scale is therefore different and the difference between the local and global results is less visible. Figure Fig. 6e shows this difference, which is comparable to what is observed for ions. This is expected, because all the difference is due to a frictional coupling to the various ion species with modified flow speeds, as direct finite orbit width effects are negligible for electrons. Since we have a weak ion temperature pedestal, the modifications of the ion flows are not sufficient to cause an appreciable deviation of the boot-

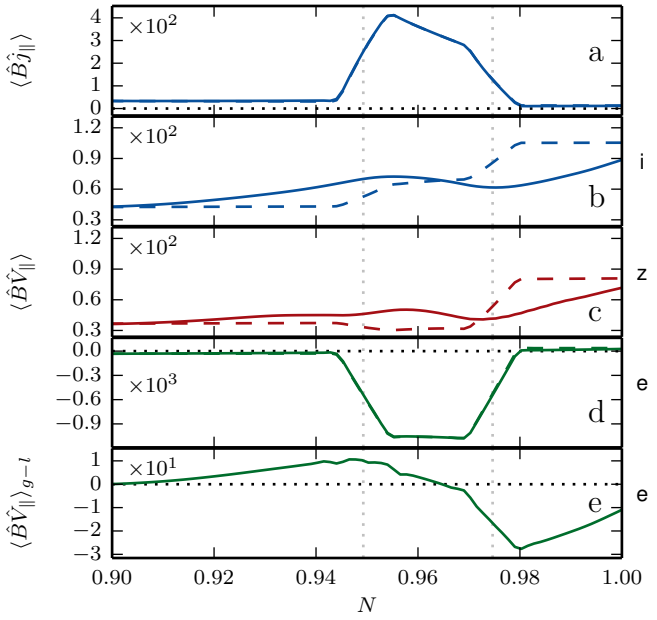

FIG. 6: $\langle BV_\parallel \rangle$ for the different species (b-d), and the parallel current these add up to (a). Solid (dashed) lines represent global (local) simulation. The difference between the global and local electron parallel flows is shown in (e). Species is indicated to the right of the panels.

strap current from the local result inside the pedestal, as seen in Fig. 6a. If anything, outside the pedestal there is a slight difference between the local and global results (barely visible on the scale accommodating the huge bootstrap peak in the pedestal), since the electron flow is relatively small in those regions, while the global effects on $k_\parallel$ extend outside the pedestal.

B. Non-trace impurities

We want to assess whether, and how, non-trace impurities can affect collisional transport in the pedestal. To this end, we performed simulations with profiles similar to our baseline, except that we scaled the impurity concentration profiles. The simulations shown in this section have impurity concentrations such that the impurity strength in the core is either $\alpha = 0.0171$ (trace impurities; shown with thin lines in the figures) or $\alpha = 1.33$ (non-trace; thick lines); as a comparison $\alpha = 0.3925$ for the baseline. Note that n_z/n_i drops rapidly across the pedestal, thus the impurities eventually become trace even if they have a high core concentration (this is necessary in the presence of an electron density pedestal if we restrict profile variations to obey the orderings of (5) for all ion species).

The a-c panels of Fig. 7 compare the local and global particle fluxes with trace and non-trace impurity concentration. As usual, the local and global results for $\hat{\Gamma}_e$ are

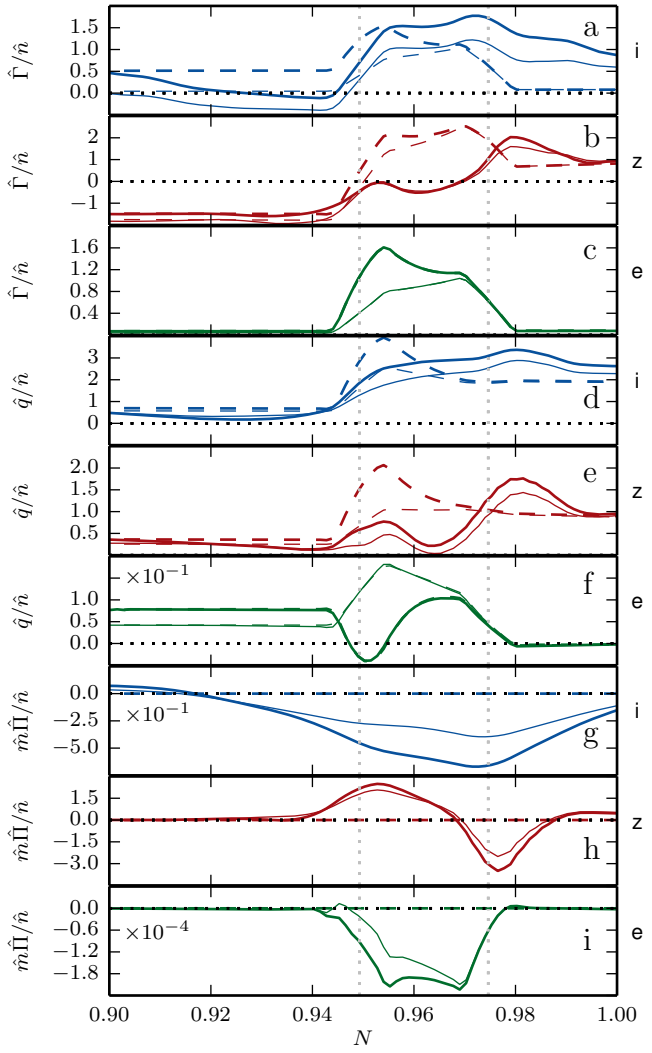

FIG. 7: Particle (a-c), heat (d-f) and momentum (g-i) fluxes divided by the normalized density for the various species. Solid (dashed) lines represent global (local) simulations, and thick (thin) lines correspond to $\alpha = 1.33$ ($\alpha = 0.0171$). Species is indicated to the right of the panels.

virtually the same. At higher impurity content the increase in $\hat{\Gamma}_e/\hat{n}_e$ around $\psi_N = 0.95$ reflects the increased n_e gradient due to the rapidly varying impurity concentration (note that n_i is kept fixed in the impurity scan, thus the n_e profile changes). The local $\hat{\Gamma}_i$ behaves as expected from the ambipolarity condition: it increases with impurity content in the core to balance the inward $\hat{\Gamma}_z$, and its core behavior is dominated by following the outward electron flux. It is interesting to note that while above $\psi_N = 0.97$ the local curves for different impurity concentration collapse onto each other because of the low n_z/n_i, the difference in the global $\hat{\Gamma}_i/\hat{n}_i$ survives much further out in the pedestal.

The d-f panels of Fig. 7 show the heat fluxes. In the

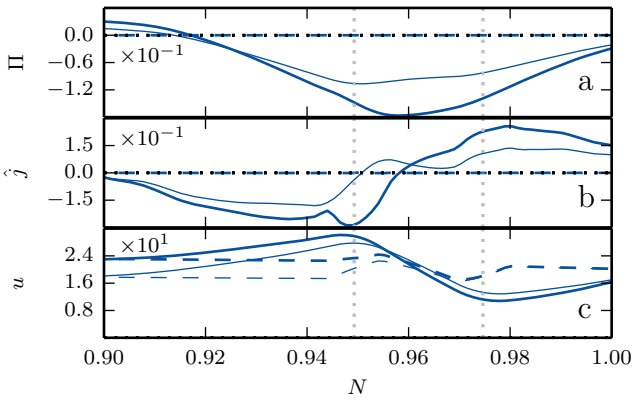

FIG. 8: Total momentum flux (a), radial current (b) and parallel mass flow (c). Thick (thin) lines correspond to $\alpha = 1.33$ ($\alpha = 0.0171$).

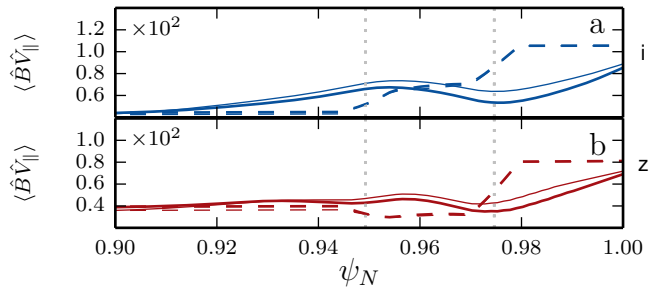

FIG. 9: $\langle BV_\parallel \rangle$ for ions and impurities. Solid (dashed) lines represent global (local) simulations, and thick (thin) lines correspond to $\alpha = 1.33$ ($\alpha = 0.0171$). Species is indicated to the right of the panels.

core and close to the pedestal top the global results for q_i are lower than the local values. This reduction is somewhat stronger in the presence of impurities. The local results for $\hat{\Gamma}_z$ and $\hat{q}_z$ are even higher in the pedestal at high impurity concentration, than would be expected simply due to the linear increase with $\hat{n}_z$. This extra increase is reduced by the global effects so that the global results at different concentrations are closer to each other.

The momentum flux values for the different species (shown in Fig. 7g-i) vanish in the local limit, as they should, but are finite when global effects are considered. Unlike $\hat{\Gamma}_e$ and $\hat{q}_e$, the global results for $\hat{\Pi}_e$ are different to the local ones, i.e. they are also finite, although the electrons do not transport an appreciable amount of momentum, as $m_e/m_i \ll 1$. The total momentum flux, $\Pi = \sum_a \hat{m}_a \hat{\Pi}_a$, shown in Fig. 8a, is mostly negative in the studied radial range, and is strongly increase by the presence of non-trace impurities. The ions are responsible for most of the momentum transport for both impurity concentrations, thus the increase in $|\Pi|$ is not due to the increase in $|\hat{\Pi}_z|$, but the modifications in $\hat{\Pi}_i$ in the presence of impurities.

The radial current $\hat{j} = \sum_a Z_a \hat{\Gamma}_a$ (Fig. 8b) – that in isolation from other transport channels would lead to charge separation and the evolution of the radial electric field – is also significantly increased in magnitude by the presence of the impurities over most of the studied radial domain. Although we observe a finite radial neoclassical current, we do not attempt to self-consistently calculate the radial electric field. For the interpretation of the momentum fluxes and the radial current it is useful to note that conservation of particle number and parallel momentum (in steady state, for a radially constant V', and with sources even in $v_\parallel$) imply that $\mathrm{d}\hat{\Gamma}_a/\mathrm{d}\psi_N \propto \hat{T}^{3/2}\hat{S}_{pa}$ and $\mathrm{d}\Pi/\mathrm{d}\psi_N \propto \hat{j}$. The latter property is apparent from a comparison of Fig. 8a and b. The former relation states that non-ambipolar fluxes require particle sources for which $\sum_a Z_a \hat{S}_{pa} = 0$ is not satisfied locally (the factor $\hat{T}^{3/2}$ comes from the assumed velocity space structure of S_{pa}).

In radially local formalisms momentum transport is often decomposed into diffusive ($\propto -\mathrm{d}u_a/\mathrm{d}\psi_N$, where $u_a = \hat{n}_a \langle \hat{B}\hat{V}_{\parallel a} \rangle \hat{m}_a$ is the normalized parallel mass flow), conductive ($\propto u_a$) and intrinsic (independent of u_a) terms. Such a decomposition is not possible in our global formalism since the parallel mass flow is a non-local function of the various plasma parameter profiles, and so is the momentum transport. Nevertheless, it is instructive to compare the radial profile of the total momentum transport Π to the radial variation of the total mass flow $u = \sum_a u_a$ shown in Fig. 8c (both quantities are dominated by the main ion contributions). By increasing the impurity content, u increases in the core region. This is caused by the higher $\hat{n}_z \langle \hat{B}\hat{V}_{\parallel z} \rangle$ at higher $\hat{n}_z$ not being compensated by the slight reduction in $\langle \hat{B}\hat{V}_{\parallel i} \rangle$ (shown in Fig. 9). As the impurity concentration drops radially across the pedestal, the effect from the reduction in the parallel ion flow becomes dominant. The radial drop in the global results for u across the pedestal is mostly due to the density variation in the pedestal. If the transport was local and purely diffusive this non-monotonic behavior of u would be accompanied by a sign change in the momentum transport. It is also interesting to note that at the point where we see the greatest relative increase in $|\Pi|$ between the different simulations ($\psi_N \approx 0.96$), the global u becomes lower for higher core impurity concentration.

The ion particle source profile shown in Fig. 10a is only weakly affected by the presence of non-trace impurities. In the meantime, the increase in impurity sources are approximately proportional to the increase in their concentration: the normalized particle source $\hat{S}_p(n_i/n_z)|_{\mathrm{core}}$ is approximately the same in the two simulations, considering that the impurity content changes by a factor 100.

The radial current and the non-quasineutral particle sources S_{pa} are consistent, that is, the divergence of the radial current is given by the charge source $\sum_a Z_a S_{pa}$ (note, that the total charge source integrated across the

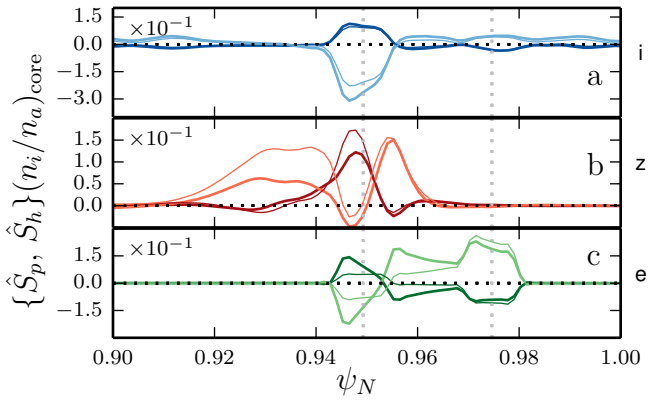

FIG. 10: Particle (dark curves) and heat (light curves) sources normalized by the species concentration in the core. Thick (thin) lines correspond to $\alpha = 1.33$ ($\alpha = 0.0171$). Species is indicated to the right of the panels.

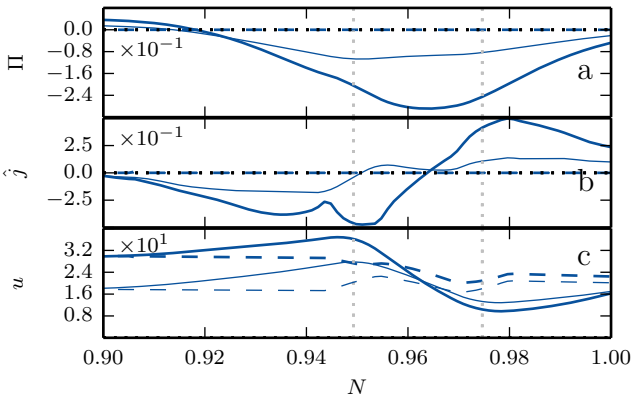

FIG. 11: Total momentum flux (a), radial current (b) and parallel mass flow (c) for beryllium impurity with modified η profiles that make the impurity density profile less steep. Thick (thin) lines correspond to $\alpha = 1.33$ ($\alpha = 0.0171$).

pedestal is zero, due to the boundary conditions). However, the radial current is truly a consequence of the radial coupling in the global simulation, and not an artifact of the radially varying sources. Although it is not done in the code, source profiles could be calculated in the presence of the radially varying *local* particle and heat fluxes, for these to be consistent with the time independent plasma parameter profiles. Such sources would be quasineutral unlike those in the global simulations.

In reality, the neoclassical radial current that we observe needs to be balanced by an opposing radial current, which represents transport processes not captured by our model (turbulence, atomic physics processes, orbit losses, magnetic ripple effects, etc.). Otherwise the system would not be steady state, because the radial electric field would vary in time and the $\mathbf{j} \times \mathbf{B}$ torque would change the plasma flows. Due to the construction of the code and the vanishing $v_\parallel$ moment of our sources, we observe the $(1/V')d(V'\Pi)/d\psi$ and the radial current terms in the species-summed flux surface averaged angular momentum equation to exactly balance. Similarly, the finite neoclassical momentum transport predicted by the code should also be canceled by a momentum transport due to non-neoclassical processes, in steady state.

Finally we would like to assess how much our profile choices affect the observation of increased momentum flux in the presence of non-trace impurities. One unnatural feature of our impurity density profile is its extreme steepness. Allowing η_i have a radial drop across the pedestal – within what is allowed by (5) – to reduce the inward radial electric field, together with allowing η_z to have an increase in the same region, leads to a less sharp impurity pedestal. To further reduce the impurity density gradient in the pedestal we consider a fully ionized beryllium impurity ($Z = 4$). These changes make our pedestal less deeply sub-sonic, as seen from the increased mass flow in Fig. 11c that shows the results of the modified input profiles. From Fig. 11a we can conclude that impurities also significantly increase the magnitude of the neoclassical momentum flux in the pedestal for more natural impurity profiles, when the inputs push the limitations imposed by the required orderings.

IV. DISCUSSION AND CONCLUSIONS

We have studied the differences in the collisional transport between radially local and global formalisms using the global δf neoclassical solver PERFECT, with a special emphasis on the effects of non-trace impurities. If the impurity density profile is arbitrary, impurities are likely to develop sonic flows and strong poloidal asymmetries in the pedestal. We use model profiles specifically chosen to guarantee that impurity flows remain sub-sonic, so that the assumptions of the δf formalism are valid. In this way we can gain some insights into the effect of non-trace impurities without the need for a non-linear collision operator.

In an impure plasma the electron particle transport is usually negligible, and the ion and impurity fluxes oppose each other to maintain ambipolarity. However, since in the pedestal the magnitude of the parallel electron flow can be much larger than the parallel ion and impurity flows, the friction of the various ion species on electrons can become non-negligible. Consequently, a substantial neoclassical electron particle transport can arise, which competes with the radial transport of other species. In particular, the ion and impurity fluxes can have the same sign. In the presence of strong radial profile variations on the ρ_{pi} scale, the ambipolarity of fluxes is violated, as reported in previous studies[18]. We emphasize that the differences in neoclassical flows and fluxes between the local and global theory are not restricted to the pedestal region only but die off within a distance comparable with

the ion orbit width. In our baseline from the outer core region to the pedestal top we observe that both the ion and impurity fluxes are inward due to global effects (see Fig. 2a-c). Inside the pedestal, local simulations predict both the impurity and the ion fluxes to be outward, due to the large outward electron flux, but in global simulations the impurity flux reverses to be inward.

For our model profiles, chosen to give small parallel ion flows, the bootstrap current remains almost completely unaffected, while this need not be so if the ion temperature varies more rapidly than allowed by our orderings. Indeed, the neoclassical parallel flow coefficient $k_\parallel$ of ions and impurities is significantly affected by global effects. Due to the radial coupling even the sign of $k_{\parallel i}$ is different from the local result well inside of the pedestal top.

We observe that in the presence of global effects the poloidal variation of the density perturbation is not restricted to an up-down asymmetry, it can be more significant, and can develop rapid radial variations (in accordance with previous numerical results[27,30]). The poloidal asymmetries observed here arise in the presence of finite inverse aspect ratio and finite orbit width effects, and are not closely related to those predicted by the analytical theories in[19,28,29], since those require significant poloidal variations in the ion-impurity friction. The adiabatic response to the electrostatic perturbation generated by the ions competes with non-adiabatic contributions in determining the poloidal asymmetries developed by the impurities. For the moderate impurity charge considered here ($Z_z = 7$) the relative poloidal variation of the impurity density is still small so that the perturbative treatment remains valid. At sufficiently high Z the relative poloidal variation of the impurity density is expected to become order unity and then – if the impurities are non-trace – nonlinear effects would start to play a role. The numerical investigation of that situation is left for a future study.

In the pedestal, the neoclassical radial current does not vanish in general, and the momentum transport remains finite – in contrast to the local theory. In the vicinity of the pedestal the total neoclassical momentum transport is found to be negative in the studied case, which happens if the charge sources (resulting from the particle sources needed to sustain the pedestal) are mostly positive in that region. The radial variation of the parallel mass flow is non-monotonic with a sharply decreasing feature where the density drops in the pedestal. This non-monotonicity is not reflected in the radial momentum transport, which is now a non-local function of the mass flow. A simple decomposition of the momentum transport into diffusive, conductive and intrinsic terms is not possible in the global picture. Note that the same is also true for all the radial fluxes.

We observe a strong effect of impurities on the total momentum transport, the magnitude of which increases significantly in the presence of non-trace impurities (see Fig. 8a). While it is not possible to disentangle the exact cause of this, it may be due to the sharp radial variation of the parallel impurity mass flow. The impurities represent only a minor fraction of the total mass flow, but their collisional coupling to the main ions is significant at an impurity strength of order unity. Pushing the limitations of our orderings we reduced the sharpness of the impurity density profile, in an attempt to demonstrate the robustness of the impact of impurities on neoclassical momentum transport. Although the impurity profile is chosen to be very specific, strong effects may occur when the impurities have more general density variations, especially because they then have much stronger relative flow speeds compared to the ions.

Impurity seeding in tokamaks operating with ITER-like metallic walls has been experimentally found to have beneficial effects on the pedestal performance. It is then natural to raise the question of whether our results are consistent with this observation. Without taking into account other non-intrinsically ambipolar processes and turbulent transport it is not possible to evolve the profiles towards a steady state. However, we may speculate about possible consequences of the increased momentum transport in the presence of impurities. In steady state the neoclassical radial current and momentum transport should be balanced by opposing contributions of turbulent and other origin. An increased neoclassical momentum transport in the presence of impurities requires these contributions to increase as well. Sufficiently far from the open field line region the turbulent transport can dominate these opposing contributions. Impurities tend to reduce the turbulence level by dilution[31–33]. If the non-diffusive turbulent momentum transport is to be increased in spite of dilution effects, stronger deviations of the non-fluctuating distribution from a Maxwellian[34] and stronger profile variations[35] may be necessary; which could require a steepening of the pedestal to reach a new steady state. Whether this is indeed the case and, if so, its role in the observed confinement improvement in impurity seeded discharges, remains an open question and should be the basis of future investigation.

ACKNOWLEDGMENTS

The authors are grateful for J. Omotani, T. Fülöp and S. Newton for fruitful discussions and instructive comments on the paper. IP and SB were supported by the International Career Grant of Vetenskapsrådet (Dnr. 330-2014-6313), and ML was supported by the U.S. DoE under award numbers DEFG0293ER54197 and DEFC0208ER54964. The simulations used computational resources of Hebbe at C3SE (project nr. C3SE2016-1-10 and SNIC2016-1-161).

Appendix A: The construction of model pedestal profiles

Here, we describe a method to construct appropriate densities given T_a, η_z, η_i profiles satisfying (5), and an

arbitrary n_i. The orderings for the electrons are not a concern, since ρ_{pe} is much smaller than the radial scale length of any profile in an experiment.

The density profiles and potential discussed in this section are the inputs to PERFECT and are thus, strictly speaking, only the zeroth order contributions to these quantities, assumed to be flux functions.

Once we have specified both η_i and n_i (to be detailed shortly), the relation $\eta_a = n_a e^{e_a \Phi / T_a}$ gives the potential

$$\Phi_0 = \frac{T_i}{e_i} \log\left(\frac{\eta_i}{n_i}\right). \tag{A1}$$

A strong electric field from Φ_0 compensates for the potentially large ion pressure drop to make the variation of η_i small (the situation of "electrostatic ion confinement," which is borne out in experimental results[36,37]). In the radial force balance the ion pressure drop could in principle be balanced by a sonic ion flow, however we consider sub-sonic ion flows. Note that by allowing sonic ion flows, the relative flow speed of two ion species would in general also be sonic, which would severely complicate the treatment of collisions. Such a scenario is currently not supported by PERFECT. We emphasize that Φ_0 and n_a are fundamental inputs to the code, thus the relation (A1) is not an attempt to self-consistently calculate the potential.

Then, given Φ_0 from (A1) and an η_z, we obtain the impurity density

$$n_z = \eta_z \left(\frac{n_i}{\eta_i}\right)^{\frac{e_z T_i}{e_i T_z}}. \tag{A2}$$

Note that (A2) leads to impurity density profiles with a typical logarithmic density gradient in the pedestal Z_z times larger than that of the main ions; this is unavoidable if (5) is to be satisfied for all ion species. Finally, the electron density is obtained by demanding quasi-neutrality

$$n_e = Z_i n_i + Z_z n_z. \tag{A3}$$

The resulting η_e satisfies (5) by virtue of the electron gyroradius being small.

Although we have constraints and relations between profiles, we still have a large degree of freedom in specifying them. Here we discuss some specific choices we made for the profile set used as a baseline for the simulations.

Since we use the local solution for the boundary condition, we also need to make sure that the assumptions of the local theory are satisfied at the boundary. This means that the sharp density or potential variations should be limited to the middle of the radial domain, sufficiently far from the boundaries. For weak electric fields the local and global results should agree, so we choose the η_i profile so that the potential calculated from (A1) is completely flat at the boundaries. We do this by letting

$$\eta_i = n_i \tag{A4}$$

in the vicinity of the inner boundary, namely in the core up to the pedestal top where n_i (and so η_i) should be slowly varying. Thus $\Phi_0 = 0$ in this region, independent of the T_i profile. To achieve a flat potential in the vicinity of the outer boundary, we let

$$\eta_i = n_i \exp\left(C/T_i\right), \tag{A5}$$

in that region, where C is a constant which fixes the value of $e\Phi_0$. To remove the ambiguity of η_i far from the boundaries in a way that makes it a simple and smooth function, we linearly extrapolate η_i given by (A4) from the core region up to the bottom of the pedestal (where the sharp feature in n_i ends) and match it to the other expression (A5), choosing $C = e\Phi_0$ from (A1) at the matching point.

The η_z profile is chosen to be a linear function of ψ over the whole domain, with a logarithmic gradient matching that of n_i at the left boundary.

Since the global δf ordering does not allow an ion temperature pedestal, we consider $T_i = T_z$ profiles with a gradient across the pedestal (and further out) equal to that of the electron temperature gradient in the core. Due to the density drop in the pedestal and the decreasing temperature profile, the ion heat flux is bound to be vastly different at the two boundaries, requiring large heat sources in the domain, except if a variation in $\mathrm{d}T_i/\mathrm{d}\psi$ balances them. This can be avoided by setting a proxy for the heat fluxes, $\propto n_i T_i^{3/2} \mathrm{d}T/\mathrm{d}\psi$, to be equal at the boundaries. Thus, we artificially reduce $\mathrm{d}T_i/\mathrm{d}\psi$ in the core to remove the need for sources close to the boundaries.

Experimental density and temperature profiles can drop orders of magnitude across the pedestal, and a significant part of these variations occur in the open field line region. As an additional consideration, if we let the bulk densities and temperatures drop across the simulation domain as much as in a real pedestal, it would lead to difficulties related to large logarithmic gradients, and huge changes in collision frequency. Since the code does not capture the physics in the open field line region (where the pedestal foot would be in an experiment), the region outside the middle of the pedestal does not carry too much physical relevance and can be considered as a numerical buffer zone. To avoid the above mentioned complications we reduce the gradients starting from a point where crossing the separatrix would be expected in an experiment. We thus arbitrarily pick this reduced $\mathrm{d}T_e/\mathrm{d}\psi$ to be 0.05 of its pedestal value, with $\mathrm{d}n_i/\mathrm{d}\psi$ equal to its core value.

Motivated by typical JET discharges (Figure 16 of 24), for our baseline case we choose the T_e and n_i pedestal widths to be $\sim 3\,\mathrm{cm}$, with the values $T_e = 0.9\,\mathrm{keV}$ and $n_e = 4 \cdot 10^{19}\,\mathrm{m}^{-3}$ at the pedestal top. These correspond to typical logarithmic gradients of about $-\mathrm{d}(\ln n_e)/\mathrm{d}(r/a) = 32.55$ and $-\mathrm{d}(\ln T_e)/\mathrm{d}(r/a) = 32.56$, where r is the minor radius defined as half of the width of the flux surface at the elevation of its centroid, and $r = a$ at the last closed flux surface. The T_e and n_i

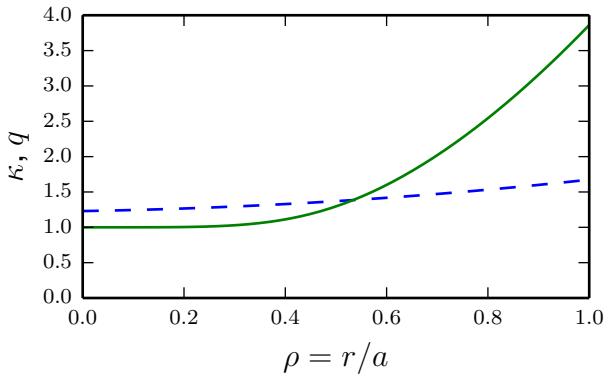

FIG. 12: q (solid curve) and κ (dashed) profiles used to calculate $\psi(r)$.

profiles are generated by Bezier curve interpolation between three regions with linear profile variation: a core, a pedestal, and an outer "buffer" region. (Using this type of smoothing ensures that the gradients transition smoothly and monotonically.)

To transform the profiles from r to ψ_N space, $\psi(r)$ is needed. This we obtain from $q(r) = \mathrm{d}\chi/\mathrm{d}\psi$ where $2\pi\chi$ is the toroidal magnetic flux which we calculate assuming simple elongated flux surfaces. Since we do not intend to model a specific experiment, we take model profiles for the safety factor q and the elongation κ, shown in Fig. 12. The q_{95} was chosen as 3.5. For the on-axis toroidal magnetic fields we take $B_t = 2.9\,\mathrm{T}$ and neglect ϵ^2 corrections together with higher order shaping effects to get $\mathrm{d}r/\mathrm{d}\psi_N$. The resulting $\mathrm{d}r/\mathrm{d}\psi_N|_{\mathrm{LCFS}} = 0.57$ is taken to be constant across the entire pedestal.

The ion temperature gradient, the ion and impurity η and the impurity strength profiles are shown in Fig. 13, for the different impurity concentration simulations presented in this paper.

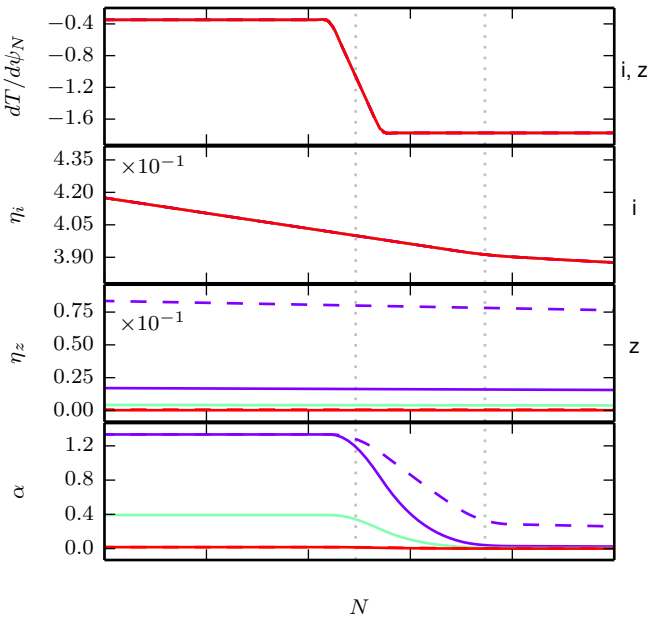

FIG. 13: Ion temperature gradient [keV], η [$10^{20}\mathrm{m}^{-3}$], and impurity strength profiles for the different simulations presented in this paper: higher impurity density (violet), baseline (cyan), trace impurity (red). Dashed lines correspond to the beryllium case of Fig. 11. Species is indicated to the right of the panels.

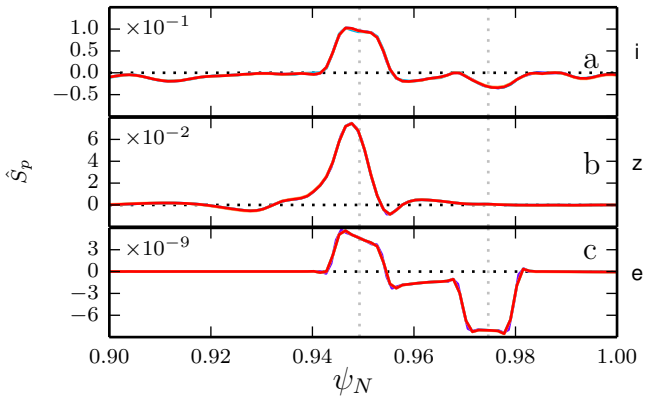

FIG. 14: The particle sources from a baseline simulation (red), plotted alongside simulations with $N_\xi = 30$ (cyan), $N_\theta = 90$ (blue), $N_\psi = 255$ (violet), radial domain size $\psi_N \in [0.825, 1.125]$ (yellow). Species is indicated to the right of the panels.

Appendix B: Numerical resolution

The simulations used $N_\psi = 204$ radial grid points and cover a domain of $\psi_N = 0.85 - 1.1$ (the whole ψ_N domain is not shown in the figures). The number of poloidal grid points is $N_\theta = 75$. The number of expansion polynomials in the pitch angle cosine $\xi = v_\parallel/v$ is $N_\xi = 24$ for the distribution function and $N_\xi^{\mathrm{RP}} = 4$ for the Rosenbluth potentials (RP). The number of speed grid points is $N_x = 8$ and $N_x^{\mathrm{RP}} = 150$ for the RP.

To demonstrate the degree of convergence, in Fig. 14 we present the particle sources for the baseline simulation for the above mentioned resolution (red curve), together with four other cases, where we increase N_ψ to 255 (violet), N_θ to $N_\theta = 90$ (blue), N_ξ to 30 (cyan), and the radial domain size to $\psi_N \in [0.825, 1.125]$ (yellow), with all other parameters kept fixed. These four are the resolution parameters to which the accuracy of the solution is most sensitive. The results are almost identical except for slight differences near sharp features.

To quantify the error, we define $\mathrm{err}(X_1) = \left(\int_{0.9}^{1} |X_2 - X_1| d\psi_N\right) / \left(\int_{0.9}^{1} |X_1| d\psi_N\right)$. Taking the $N_\psi = 255$ simulation as the reference X_2, we find that the quantity with the highest error is the electron particle source, with $\mathrm{err}(\hat{S}_{pe}) = 5.6\%$. For other quantities, such as particle flows and radial fluxes, we observe errors

below 0.5%, thus Fig. 14 presents the most stringent test for numerical convergence. The same convergence test was performed for all the simulations, with resulting errors (including those of the sources) all being below 6%.

[1] A. E. Hubbard, "Physics and scaling of the H-mode pedestal," Plasma Physics and Controlled Fusion **42**, A15 (2000).

[2] R. J. Groebner, A. W. Leonard, T. C. Luce, M. E. Fenstermacher, G. L. Jackson, T. H. Osborne, D. M. Thomas, and M. R. Wade, "Comparison of H-mode pedestals in different confinement regimes in DIII-D," Plasma Physics and Controlled Fusion **48**, A109 (2006).

[3] P. W. Terry, "Suppression of turbulence and transport by sheared flow," Rev. Mod. Phys. **72**, 109–165 (2000).

[4] E. G. Highcock, A. A. Schekochihin, S. C. Cowley, M. Barnes, F. I. Parra, C. M. Roach, and W. Dorland, "Zero-turbulence manifold in a toroidal plasma," Phys. Rev. Lett. **109**, 265001 (2012).

[5] M. N. A. Beurskens, J. Schweinzer, C. Angioni, A. Burckhart, C. D. Challis, I. Chapman, R. Fischer, J. Flanagan, L. Frassinetti, C. Giroud, J. Hobirk, E. Joffrin, A. Kallenbach, M. Kempenaars, M. Leyland, P. Lomas, G. Maddison, M. Maslov, R. McDermott, R. Neu, I. Nunes, T. Osborne, F. Ryter, S. Saarelma, P. A. Schneider, P. Snyder, G. Tardini, E. Viezzer, E. Wolfrum, the ASDEX Upgrade Team, and JET-EFDA Contributors, "The effect of a metal wall on confinement in JET and ASDEX Upgrade," Plasma Physics and Controlled Fusion **55**, 124043 (2013).

[6] M. Beurskens, L. Frassinetti, C. Challis, C. Giroud, S. Saarelma, B. Alper, C. Angioni, P. Bilkova, C. Bourdelle, S. Brezinsek, P. Buratti, G. Calabro, T. Eich, J. Flanagan, E. Giovannozzi, M. Groth, J. Hobirk, E. Joffrin, M. Leyland, P. Lomas, E. de la Luna, M. Kempenaars, G. Maddison, C. Maggi, P. Mantica, M. Maslov, G. Matthews, M.-L. Mayoral, R. Neu, I. Nunes, T. Osborne, F. Rimini, R. Scannell, E. Solano, P. Snyder, I. Voitsekhovitch, P. de Vries, and JET-EFDA Contributors, "Global and pedestal confinement in JET with a Be/W metallic wall," Nuclear Fusion **54**, 043001 (2014).

[7] L. Frassinetti, D. Dodt, M. Beurskens, A. Sirinelli, J. Boom, T. Eich, J. Flanagan, C. Giroud, M. Jachmich, M. Kempenaars, P. Lomas, G. Maddison, C. Maggi, R. Neu, I. Nunes, C. P. von Thun, B. Sieglin, M. Stamp, and JET-EFDA Contributors, "Effect of nitrogen seeding on the energy losses and on the time scales of the electron temperature and density collapse of type-I ELMs in JET with the ITER-like wall," Nuclear Fusion **55**, 023007 (2015).

[8] G. Kagan, *Finite drift orbit effects in a tokamak pedestal*, Ph.D. thesis, Massachusetts Institute of Technology (2009).

[9] G. Kagan and P. J. Catto, "Arbitrary poloidal gyroradius effects in tokamak pedestals and transport barriers," Plasma Physics and Controlled Fusion **50**, 085010 (2008).

[10] G. Kagan and P. J. Catto, "Neoclassical ion heat flux and poloidal flow in a tokamak pedestal," Plasma Physics and Controlled Fusion **52**, 055004 (2010).

[11] G. Kagan and P. J. Catto, "Enhancement of the bootstrap current in a tokamak pedestal," Phys. Rev. Lett. **105**, 045002 (2010).

[12] I. Pusztai and P. J. Catto, "Neoclassical plateau regime transport in a tokamak pedestal," Plasma Physics and Controlled Fusion **52**, 075016 (2010).

[13] P. J. Catto, G. Kagan, M. Landreman, and I. Pusztai, "A unified treatment of kinetic effects in a tokamak pedestal," Plasma Physics and Controlled Fusion **53**, 054004 (2011).

[14] P. J. Catto, F. I. Parra, G. Kagan, J. B. Parker, I. Pusztai, and M. Landreman, "Kinetic effects on a tokamak pedestal ion flow, ion heat transport and bootstrap current," Plasma Physics and Controlled Fusion **55**, 045009 (2013).

[15] J. Candy and E. A. Belli, "Neoclassical transport including collisional nonlinearity," Phys. Rev. Lett. **106**, 235003 (2011).

[16] S. Koh, C. S. Chang, S. Ku, J. E. Menard, H. Weitzner, and W. Choe, "Bootstrap current for the edge pedestal plasma in a diverted tokamak geometry," Physics of Plasmas **19**, 072505 (2012), http://dx.doi.org/10.1063/1.4736953.

[17] J. Seo, C. S. Chang, S. Ku, J. M. Kwon, W. Choe, and S. H. Müller, "Intrinsic momentum generation by a combined neoclassical and turbulence mechanism in diverted DIII-D plasma edge," Physics of Plasmas **21**, 092501 (2014), http://dx.doi.org/10.1063/1.4894242.

[18] M. Landreman, F. I. Parra, P. J. Catto, D. R. Ernst, and I. Pusztai, "Radially global δf computation of neoclassical phenomena in a tokamak pedestal," Plasma Physics and Controlled Fusion **56**, 045005 (2014), arXiv:1312.2148 [physics.plasm-ph].

[19] T. Fülöp and P. Helander, "Nonlinear neoclassical transport in toroidal edge plasmas," Physics of Plasmas **8**, 3305 (2001).

[20] X. Q. Xu, "Neoclassical simulation of tokamak plasmas using the continuum gyrokinetic code TEMPEST," Phys. Rev. E **78**, 016406 (2008).

[21] M. A. Dorf, R. H. Cohen, M. Dorr, T. Rognlien, J. Hittinger, J. Compton, P. Colella, D. Martin, and P. McCorquodale, "Simulation of neoclassical transport with the continuum gyrokinetic code COGENT," Physics of Plasmas **20**, 012513 (2013), http://dx.doi.org/10.1063/1.4776712.

[22] M. Dorf, M. Dorr, R. Cohen, T. Rognlien, and J. Hittinger, "Modeling of ion orbit loss and intrinsic toroidal rotation with the COGENT code," Bulletin of the American Physical Society, 56th Annual Meeting of the APS Division of Plasma Physics (New Orleans, LA, USA) **59**, "TP8.00027" (2014).

[23] T. Fülöp, P. Helander, and P. J. Catto, "Effect of poloidal density variation of neutral atoms on the tokamak edge," Phys. Rev. Lett. **89**, 225003 (2002).

[24] C. Maggi, S. Saarelma, F. Casson, C. Challis, E. de la Luna, L. Frassinetti, C. Giroud, E. Joffrin, J. Simpson, M. Beurskens, I. Chapman, J. Hobirk, M. Leyland, P. Lomas, C. Lowry, I. Nunes, F. Rimini, A. Sips, and H. Urano, "Pedestal confinement and stability in JET-ILW ELMy H-modes," Nuclear Fusion **55**, 113031 (2015).

[25] R. L. Miller, M. S. Chu, J. M. Greene, Y. R. Lin-Liu, and R. E. Waltz, "Noncircular, finite aspect ratio, local equilibrium model," Physics of Plasmas **5**, 973–978 (1998).

[26] E. A. Belli, G. W. Hammett, and W. Dorland, "Effects of plasma shaping on nonlinear gyrokinetic turbulence," Physics of Plasmas **15**, 092303 (2008), http://dx.doi.org/10.1063/1.2972160.

[27] I. Pusztai, M. Landreman, A. Mollén, Y. O. Kazakov, and T. Fülöp, "Radio frequency induced and neoclassical asymmetries and their effects on turbulent impurity transport in a tokamak," Contributions to Plasma Physics **54**, 534–542 (2014).

[28] T. Fülöp and P. Helander, "Nonlinear neoclassical transport in a rotating impure plasma with large gradients," Physics of Plasmas **6**, 3066–3075 (1999).

[29] M. Landreman, T. Fülöp, and D. Guszejnov, "Impurity flows and plateau-regime poloidal density variation in a tokamak pedestal," Physics of Plasmas **18**, 092507 (2011), http://dx.doi.org/10.1063/1.3631819.

[30] M. Landreman and D. R. Ernst, "Local and global Fokker-Planck neoclassical calculations showing flow and bootstrap current modification in a pedestal," Plasma Physics and Controlled Fusion **54**, 115006 (2012).

[31] I. Pusztai, J. Candy, and P. Gohil, "Isotope mass and charge effects in tokamak plasmas," Physics of Plasmas **18**, 122501 (2011), http://dx.doi.org/10.1063/1.3663844.

[32] M. Porkolab, J. Dorris, P. Ennever, C. Fiore, M. Greenwald, A. Hubbard, Y. Ma, E. Marmar, Y. Podpaly, M. L. Reinke, J. E. Rice, J. C. Rost, N. Tsujii, D. Ernst, J. Candy, G. M. Staebler, and R. E. Waltz, "Transport and turbulence studies in the linear ohmic confinement regime in alcator c-mod," Plasma Physics and Controlled Fusion **54**, 124029 (2012).

[33] I. Pusztai, A. Mollén, T. Fülöp, and J. Candy, "Turbulent transport of impurities and their effect on energy confinement," Plasma Physics and Controlled Fusion **55**, 074012 (2013).

[34] J. Lee, F. I. Parra, and M. Barnes, "Turbulent momentum pinch of diamagnetic flows in a tokamak," Nuclear Fusion **54**, 022002 (2014).

[35] T. Sung, R. Buchholz, F. J. Casson, E. Fable, S. R. Grosshauser, W. A. Hornsby, P. Migliano, and A. G. Peeters, "Toroidal momentum transport in a tokamak caused by symmetry breaking parallel derivatives," Physics of Plasmas **20**, 042506 (2013), http://dx.doi.org/10.1063/1.4799750.

[36] E. Viezzer, *Radial electric field studies in the plasma edge of ASDEX*, Ph.D. thesis, Ludwig-Maximilians-Universität München (2013).

[37] R. M. McDermott, B. Lipschultz, J. W. Hughes, P. J. Catto, A. E. Hubbard, I. H. Hutchinson, R. S. Granetz, M. Greenwald, B. LaBombard, K. Marr, M. L. Reinke, J. E. Rice, D. Whyte, and A. C.-M. Team, "Edge radial electric field structure and its connections to h-mode confinement in Alcator C-Mod plasmas," Physics of Plasmas **16**, 056103 (2009), http://dx.doi.org/10.1063/1.3080721.